

1 Estimation of the number of synapses in the hippocampus and 2 brain-wide by volume electron microscopy and genetic labeling

3
4 **Andrea Santuy¹, Laura Tomás-Roca², José-Rodrigo Rodríguez^{1,3,4}, Juncal González-Soriano⁵,**
5 **Fei Zhu^{2,6}, Zhen Qiu², Seth GN Grant², Javier DeFelipe^{1,3,4}, Angel Merchan-Perez^{1,4,7}**

6
7 1 Laboratorio Cajal de Circuitos Corticales, Centro de Tecnología Biomédica, Universidad
8 Politécnica de Madrid, Pozuelo de Alarcón, 28223 Madrid, Spain.

9 2 Genes to Cognition Program, Centre for Clinical Brain Sciences, University of Edinburgh,
10 Edinburgh EH16 4SB, UK

11 3 Instituto Cajal, Consejo Superior de Investigaciones Científicas (CSIC), Avda. Doctor Arce, 37,
12 28002 Madrid, Spain.

13 4 Centro de Investigación Biomédica en Red sobre Enfermedades Neurodegenerativas
14 (CIBERNED) ISCIII, Madrid, Spain.

15 5 Departamento de Anatomía y Embriología, Universidad Complutense de Madrid, 28040
16 Madrid, Spain.

17 6 UCL Institute of Neurology, Queen Square, WC1N 3BG London, UK

18 7 Departamento de Arquitectura y Tecnología de Sistemas Informáticos, Universidad
19 Politécnica de Madrid, Pozuelo de Alarcón, 28223 Madrid, Spain. Corresponding author

20
21 JDF, SG and AMP designed research; AS, LTR, JRR, JGS, FZ and ZQ performed research; AS, LTR,
22 and AMP analyzed data; AS, LTR, SG, JDF and AMP wrote the paper.

23
24 **Abbreviated Title:** Brain-wide estimation of synapses

25
26 **Correspondence should be addressed to:** Angel Merchan-Perez, Laboratorio Cajal de Circuitos
27 Corticales, Centro de Tecnología Biomédica, Universidad Politécnica de Madrid, Pozuelo de
28 Alarcón, 28223, Madrid, Spain: angel.merchan@upm.es

34 **Abstract**

35 Determining the number of synapses that are present in different brain regions is crucial to
36 understand brain connectivity as a whole. Membrane-associated guanylate kinases (MAGUKs)
37 are a family of scaffolding proteins that are expressed in excitatory glutamatergic synapses.
38 We used genetic labeling of two of these proteins (PSD95 and SAP102), and Spinning Disc
39 confocal Microscopy (SDM), to estimate the number of fluorescent puncta in the CA1 area of
40 the hippocampus. We also used FIB-SEM, a three-dimensional electron microscopy technique,
41 to calculate the actual numbers of synapses in the same area. We then estimated the ratio
42 between the three-dimensional densities obtained with FIB-SEM (synapses/ μm^3) and the bi-
43 dimensional densities obtained with SDM (puncta/ $100 \mu\text{m}^2$). Given that it is impractical to use
44 FIB-SEM brain-wide, we used previously available SDM data from other brain regions and we
45 applied this ratio as a conversion factor to estimate the minimum density of synapses in those
46 regions. We found the highest densities of synapses in the isocortex, olfactory areas,
47 hippocampal formation and cortical subplate. Low densities were found in the pallidum,
48 hypothalamus, brainstem and cerebellum. Finally, the striatum and thalamus showed a wide
49 range of synapse densities.

50

51 **Keywords**

52 FIB-SEM, PSD95, SAP102, Hippocampus, CA1

53

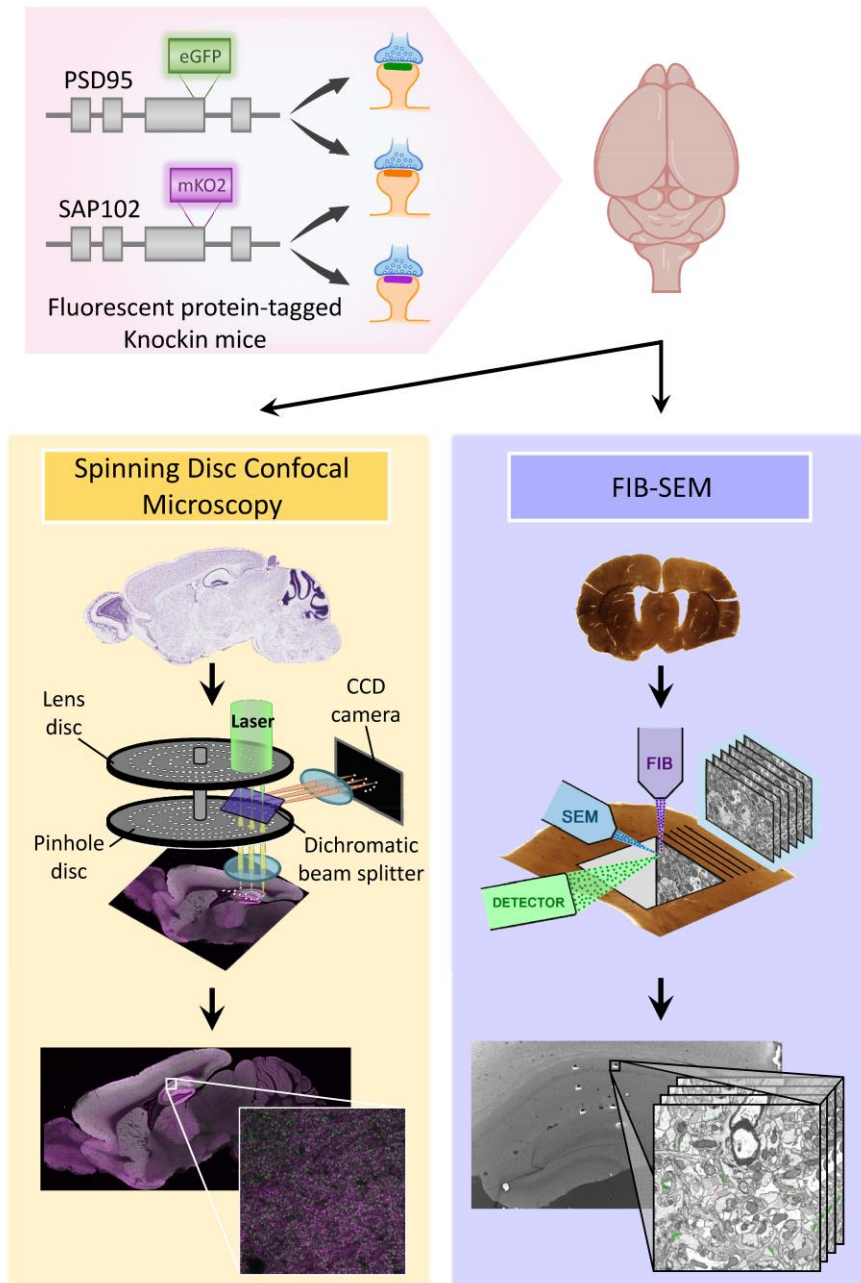
54

55 Introduction

56 Determining the number of synapses that are present in different brain regions is crucial to
57 understand brain connectivity as a whole. Synapses can be identified with several methods,
58 including genetic labeling of synaptic scaffolding proteins and electron microscopy (EM).
59 Membrane-associated guanylate kinases (MAGUKs) are a family of scaffolding proteins that
60 participate in the regulation of cell polarity, cell adhesion and synaptic signal transduction
61 (Migaud et al., 1998; Ye et al., 2018; Zhu et al., 2016). PSD95 and SAP102 belong to the
62 MAGUK family and are expressed in the postsynaptic density (PSD) of excitatory glutamatergic
63 synapses (Aoki et al., 2001; Chen et al., 2018, 2008; DeGiorgis et al., 2006; Farley et al., 2015;
64 Husi et al., 2000; Petersen et al., 2003; Valtschanoff et al., 1999; Yamasaki et al., 2016), where
65 they contribute to the recruitment and retention of glutamate receptors (Hafner et al., 2015;
66 Jeyifous et al., 2016; Levy et al., 2015). Genetic labeling of the endogenous PSD95 and SAP102
67 postsynaptic proteins and imaging using Spinning Disk confocal Microscopy (SDM) have been
68 proven to be useful for the characterization of synapse diversity in all brain regions of the
69 mouse. SDM is a rapid method that allows the imaging of entire brain sections, so the
70 simultaneous visualization of millions of synapses is made possible, obtaining bi-dimensional
71 densities of fluorescent puncta per surface area (puncta/100 μm^2) (Zhu et al., 2018).

72 Previous attempts have been made to calculate the density of synapses in the brain using EM.
73 This technique allows the identification of individual synapses, although it is restricted to much
74 smaller fields of view. Furthermore, most of these EM studies apply stereological techniques to
75 a limited number of EM sections. Although stereology is a proven valuable method for object
76 counting, the total number of synapses is an estimation which is subject to several technical
77 limitations [see (DeFelipe et al., 1999) for a review]. In the present study, we use Focused Ion
78 Beam milling-Scanning Electron Microscopy (FIB-SEM). With this technique, sectioning and
79 imaging are fully automated, allowing the acquisition of multiple serial micrographs. Later, the
80 micrographs can be stacked with the help of software tools, such that they represent a three-
81 dimensional sample of tissue (Merchán-Pérez et al., 2009). In this way, all individual synapses
82 can be identified and counted within a known volume of brain tissue, and thus the true density
83 of synapses per unit volume can be obtained directly (not through estimations using
84 stereological methods).

85 The aim of our study was twofold. First, we wanted to obtain detailed data about the density
86 and size of synapses in the hippocampus. To this end, we used SDM to measure the densities
87 of PSD95 and SAP102 puncta in stratum oriens (SO), stratum radiatum (SR) and stratum
88 lacunosum-moleculare (SLM) of CA1. We also used FIB-SEM to measure the actual density of
89 synapses in three-dimensional samples of the same strata (Figure 1). We then calculated the
90 quantitative relationship between the densities and sizes of fluorescent puncta and synapses
91 obtained by the two methods. Second, given that volume electron microscopy cannot be
92 applied brain-wide, we wanted to obtain an estimate of the number of synapses in other
93 regions of the brain where measurements of PSD95 and SAP102 puncta were available (Zhu et
94 al., 2018). We based this estimate on the quantitative relationship or conversion factor
95 between SDM and FIB-SEM data previously obtained in the hippocampus. Even though this
96 approach has several limitations and underestimates the actual numbers of synapses, it
97 provides valuable information on the *minimum* number of excitatory synapses that are present
98 in more than a hundred brain regions.



99

100 **Figure 1. General methodology.** Knockin mice expressing fluorescent PSD95 and SAP102 were
101 imaged with Spinning Disc Confocal Microscopy (SDM) and with FIB-SEM. SDM allows the
102 acquisition of large field, 2D fluorescent images, while FIB-SEM is an electron microscopy
103 technique with a resolution in the scale of nanometres that generates 3D stacks of images, but
104 with a smaller field of view. We have used a combination of both techniques to estimate the
105 actual densities of synapses per unit volume brain-wide.

106

107

108 **Materials and Methods**

109 **Animals**

110 For this study, we used adult male mice (postnatal day 56) expressing fluorescently labeled
111 PSD95 and SAP102 postsynaptic proteins (PSD95^{eGFP/eGFP}; SAP102^{mKO2/Y}) (Zhu et al., 2018). All
112 animals were handled in accordance with the guidelines for animal research set out in the
113 European Community Directive 2010/63/EU, and all procedures were approved by the Ethics
114 Committee for Animal Experimentation of the Cajal Institute (CSIC, Spain).

115 **Tissue preparation for spinning disc microscopy**

116 Sixteen mice were anesthetized by an intraperitoneal injection of 0.1 mL of 20% w/v sodium
117 pentobarbital (Euthatal, Merial Animal Health Ltd. or Pentoject, Animalcare Ltd.). After
118 complete anesthesia, 10 mL of phosphate buffered saline (PBS; Oxoid) were perfused
119 transcardially, followed by 10 mL of 4% v/v paraformaldehyde (PFA; Alfa Aesar). Whole brains
120 were dissected out and post-fixed for 3–4 h at 4 °C in 4% PFA, and then cryoprotected for 3
121 days at 4 °C in 30% sucrose solution (w/v in 1× PBS; VWR Chemicals). Brains were then
122 embedded into optimal cutting temperature (OCT) medium within a cryomould and frozen by
123 placing the mould in isopentane cooled down with liquid nitrogen. Brains were then sectioned,
124 with a thickness of 18 µm, using an NX70 Thermo Fisher cryostat, and cryosections were
125 mounted on Superfrost Plus glass slides (Thermo scientific) and stored at –80 °C.

126 **Histology and immunohistochemistry**

127 Sections were washed for 5 min in PBS, incubated for 15 min in 1 µg/mL DAPI (Sigma), washed
128 and mounted using home-made MOWIOL (Calbiochem) containing 2.5% anti-fading agent
129 DABCO (Sigma-Aldrich), covered with a coverslip (thickness #1.5, VWR international) and
130 imaged the following day.

131 **Spinning Disk Confocal Microscopy**

132 For synaptome mapping, we used Spinning Disk confocal Microscopy (SDM) platforms (Figure
133 2). The Andor Revolution XDi was used with an Olympus UPlanSAPO 100X oil immersion lens
134 (NA 1.4), a CSU-X1 spinning-disk (Yokogawa) and an Andor iXon Ultra monochrome back-
135 illuminated EMCCD camera. Images acquired with this system have a pixel dimension of 84 ×
136 84 nm and a depth of 16 bits. A single mosaic grid was used to cover each entire brain section
137 with an adaptive Z focus set-up by the user to follow the unevenness of the tissue using Andor
138 iQ2 software. The field of view of each individual frame was 43.008 x 43.008 µm. In both
139 systems, eGFP was excited using a 488 nm laser and mKO2 with a 561 nm laser. The CV1000
140 system is equipped with the following filters: BP 525/50 nm for eGFP and BP 617/73 nm for
141 mKO2, whereas the Andor Revolution XDi is equipped with a Quad filter (BP 440/40, BP
142 521/21, BP 607/34 and BP 700/45). For both systems, mosaic imaging was set up with no
143 overlap between adjacent tiles.

144 **Detection and measurement of fluorescent Synaptic Puncta**

145 Punctum detection was performed using Ensemble Detection, an in-house collection of image
146 detection algorithms. We have developed a new punctum/particle detection method based on
147 a multi-resolution image feature detector and supervised machine learning technique (Zhu et
148 al., 2018). In this method, we carry out a multi-resolution and multi-orientation version of 2nd-
149 order nonlocal derivative (NLD) (Qiu et al., 2012), and use it to calculate intensity differences,

150 referred to as ‘image features’, for each of the individual puncta at different spatial resolutions
151 and orientations. An initial intensity threshold is set to a very low value to only filter out
152 extremely dim puncta and to avoid missing true synaptic puncta. The remaining candidate
153 puncta were finally classified as either true puncta or background noise using the
154 corresponding feature vectors and the classifier. The classifier was pre-trained with the
155 training image set and machine learning algorithms (Qiu et al., 2012).

156 After detection and localization of all puncta, we segmented them based on their individual
157 intensity values: for each punctum, a threshold was set as 10% of the maximum pixel intensity
158 within the punctum, so that punctum size and shape measurement were independent of
159 punctum intensity (Zhu et al., 2018). With the puncta segmented and binarized, six punctum
160 parameters were then calculated: mean punctum pixel intensity, punctum size, skewness,
161 kurtosis, circularity, and aspect ratio.

162 **Tissue Preparation for electron microscopy**

163 Four male PSD95^{eGFP/eGFP}; SAP102^{mKO2/Y} mice were used for electron microscopy. Animals were
164 administered a lethal intraperitoneal injection of sodium pentobarbital (40 mg/kg) and were
165 intracardially perfused with 2% paraformaldehyde and 2.5% glutaraldehyde in 0.1 M
166 phosphate buffer (PB). The brain was then extracted from the skull and processed for EM as
167 previously described (Merchán-Pérez et al., 2009). Briefly, the brains were post-fixed at 4°C
168 overnight in the same solution used for perfusion. They were then washed in PB and
169 vibratome sections (150 µm thick) were obtained. Sections containing the rostral hippocampus
170 were selected with the help of an atlas (Paxinos and Franklin, 2004). Selected sections were
171 osmicated for 1 hour at room temperature in PB with 1% OsO₄, 7% glucose and 0.02 M CaCl₂.
172 After washing in PB, the sections were stained for 30 min with 1% uranyl acetate in 50%
173 ethanol at 37°C, and they were then dehydrated and flat embedded in Araldite (DeFelipe and
174 Fairén, 1993). Embedded sections were glued onto blank Araldite stubs and trimmed. To select
175 the exact location of the samples, we first obtained semithin sections (1–2 µm thick) from the
176 block surface and stained them with toluidine blue to identify cortical layers. These sections
177 were then photographed with a light microscope. The last of these light microscope images
178 (corresponding to the section immediately adjacent to the block face) was then collated with
179 low power scanning electron microscope (SEM) photographs of the surface of the block. In this
180 way, it was possible to accurately identify the three strata of the hippocampus to be studied.

181 **Three-Dimensional Electron Microscopy**

182 Three-dimensional brain tissue samples of the CA1 of the hippocampus were obtained using
183 combined focused ion beam milling and scanning electron microscopy (FIB-SEM) (Figure 3).
184 The focus of our study was the neuropil, which is composed of axons, dendrites and glial
185 processes. We used a CrossBeam 540 electron microscope (Carl Zeiss NTS GmbH, Oberkochen,
186 Germany). This instrument combines a high-resolution field emission SEM column with a
187 focused gallium ion beam, which can mill the sample surface, removing thin layers of material
188 on a nanometer scale. After removing each slice (20 nm thick), the milling process was paused,
189 and the freshly exposed surface was imaged with a 1.8-kV acceleration potential using the in-
190 column energy selective backscattered (EsB) electron detector. The milling and imaging
191 processes were sequentially repeated, and long series of images were acquired through a fully
192 automated procedure, thus obtaining a stack of images that represented a three-dimensional
193 sample of the tissue (Merchán-Pérez et al., 2009). Twelve samples (stacks of images) of the
194 neuropil of three strata of CA1 were obtained, avoiding the neuronal and glial somata as well

195 as the blood vessels (Figure 4). These stacks included four samples of stratum lacunosum
196 moleculare (SLM), four of stratum radiatum (SR) and four of stratum oriens (SO) (see
197 Supplementary Table 1). In these stacks, we obtained the densities of glutamatergic
198 (asymmetric) and GABAergic (symmetric) synaptic junctions. To do this, we counted the
199 number of synaptic junctions within an unbiased three-dimensional counting frame of known
200 volume (Howard and Reed, 2005). Image resolution in the xy plane was 5 nm/pixel; resolution
201 in the z-axis (section thickness) was 20 nm and image sizes were 2048 x 1536 pixels (field of
202 view: 10.24 x 7.68 μm). The number of sections per stack ranged from 201 to 377 (mean
203 276.33; total 3316 sections). Processing for EM causes shrinkage of the tissue for which we
204 have to correct the measurements (Merchán-Pérez et al., 2009). Correction factors for the
205 tissue that was used in this study were 0.9508 for linear measurements, 0.9040 for area
206 measurements and 0.8595 for volumetric data. The volumes of the stacks, after correction for
207 tissue shrinkage, ranged from 367.81 to 689.86 μm^3 (mean 505.66 μm^3 ; total 6067.86 μm^3).
208 The volumes of the counting frames ranged from 288.62 to 585.99 μm^3 (mean 408.76 μm^3 ;
209 total 4905.07 μm^3) (Supplementary Table 1).

210 **Identification and reconstruction of synapses**

211 Synaptic junctions within these volumes were visualized and segmented in 3D with Espina
212 software (Morales et al., 2011) (<http://cajalbbp.es/espina/>). The segmentation algorithm
213 makes use of the fact that presynaptic and postsynaptic densities appear as dark, electron-
214 dense structures under the electron microscope. It requires a Gaussian blur filter
215 preprocessing to eliminate noisy pixels and then it uses a gray-level threshold to extract all the
216 voxels that fit the gray levels of the synaptic junction. In this way, the resulting 3D
217 segmentation includes both the active zone (AZ) and postsynaptic density (PSD) (Morales et
218 al., 2013). Synaptic junctions with a prominent or thin PSD were classified as asymmetric or
219 symmetric synaptic junctions, respectively (Colonnier, 1968; Gray, 1959) (Figure 3). Synapses
220 could be unambiguously identified since they can be visualized in consecutive serial sections
221 and, if necessary, they can be digitally resectioned in different planes to ascertain their identity
222 as asymmetric or symmetric synapses (DeFelipe et al., 1999; Merchán-Pérez et al., 2009).

223 **Size of synapses**

224 As stated above, the synaptic junction is formed by the AZ and the PSD. Since AZ and PSD are
225 in close apposition and have similar surface areas, they can be represented as a single surface
226 — the synaptic apposition surface (SAS). Thus, the SAS is an accurate measurement of the size
227 of the synapse. In previous studies we have developed an efficient computational technique to
228 automatically extract this surface from reconstructed synapses (Morales et al., 2013).

229 **Statistical analysis**

230 To study whether there were significant differences between synaptic distributions among the
231 different CA1 layers, we performed a multiple mean comparison test. When the data met the
232 criteria of normality and homoscedasticity, an ANOVA was performed. When these criteria
233 were not met, we used the Kruskal-Wallis followed by Dunn's test for pair-wise comparisons.

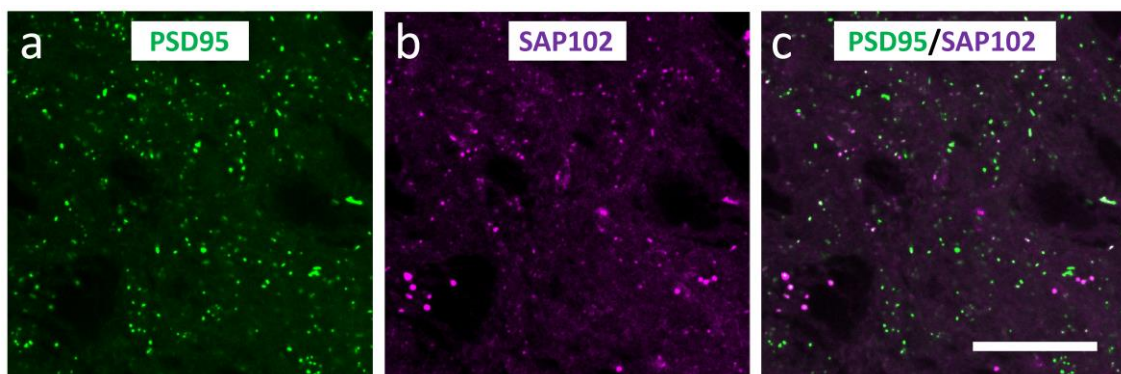
234

235

236 Results

237 We estimated the density and the size of synapses in the CA1 area of the hippocampus using
238 two different methods (Figure 1). PSD95-positive and SAP102-positive synapses were
239 identified as fluorescent puncta using SDM (Figure 2), and FIB-SEM was used to visualize and
240 reconstruct synaptic junctions in the same regions. FIB-SEM also provided information that
241 was not obtained from confocal images, such as the relative proportions of excitatory
242 (asymmetric) and inhibitory (symmetric) synapses (Figure 3, Supplementary Table 1). This
243 classification of synapses is based on the appearance of the PSD in EM images (Colonnier,
244 1968; Gray, 1959). Any synaptic junction with a dense, prominent PSD that was much thicker
245 than the relatively faint presynaptic thickening was classified as “asymmetric” (AS). Any
246 synapse with a less marked PSD, similar to the presynaptic thickening, was classified as
247 “symmetric” (SS) (Merchán-Pérez et al., 2009). It should be stressed that the classification of
248 synaptic junctions into one of these two groups was not based on the examination of single
249 sections, but on the whole series of images in which the PSD was visible (Figure 3). Once all
250 synapses within a given stack of serial sections had been identified and segmented, they
251 appeared as a cloud of 3D objects from which quantitative data were obtained (Figure 4).

252



253

254 **Figure 2. Spinning Disk confocal Microscopy (SDM).** (a and b): Examples of PSD95 fluorescent
255 puncta (green) and SAP102 puncta (purple), imaged with SDM in the stratum lacunosum-
256 moleculare of CA1. The PSD95 and SAP102 channels have been merged in (c). Calibration bar:
257 15 μm .

258

259

260 Density of fluorescent puncta and synapses in the hippocampus

261 Densities of fluorescent puncta (number of positive puncta per 100 μm^2) were measured in
262 SLM, SR and SO from CA1. Sixteen brain sections were used (one section per animal, see
263 Supplementary Table 2). We obtained the densities of puncta expressing PSD95 ($dPSD95$) and
264 SAP102 ($dSAP102$), as well as the colocalization index (c). From these data we calculated the
265 total density of puncta ($dTotal$) (Table 1, Supplementary Table 2). Note that $dTotal$ is not
266 simply the sum of $dPSD95$ and $dSAP102$, since there is a certain density of puncta that
267 colocalize ($dColoc$):

268

$$dTotal = dPSD95 + dSAP102 - dColoc$$

269 The colocalization index (c) ranges from 0, when there is no colocalization, to 1, when there is
270 100% colocalization, so $dColoc$ is related to $dTotal$ according to the following expression:

$$271 \quad dColoc = c \times dTotal$$

272 Therefore,

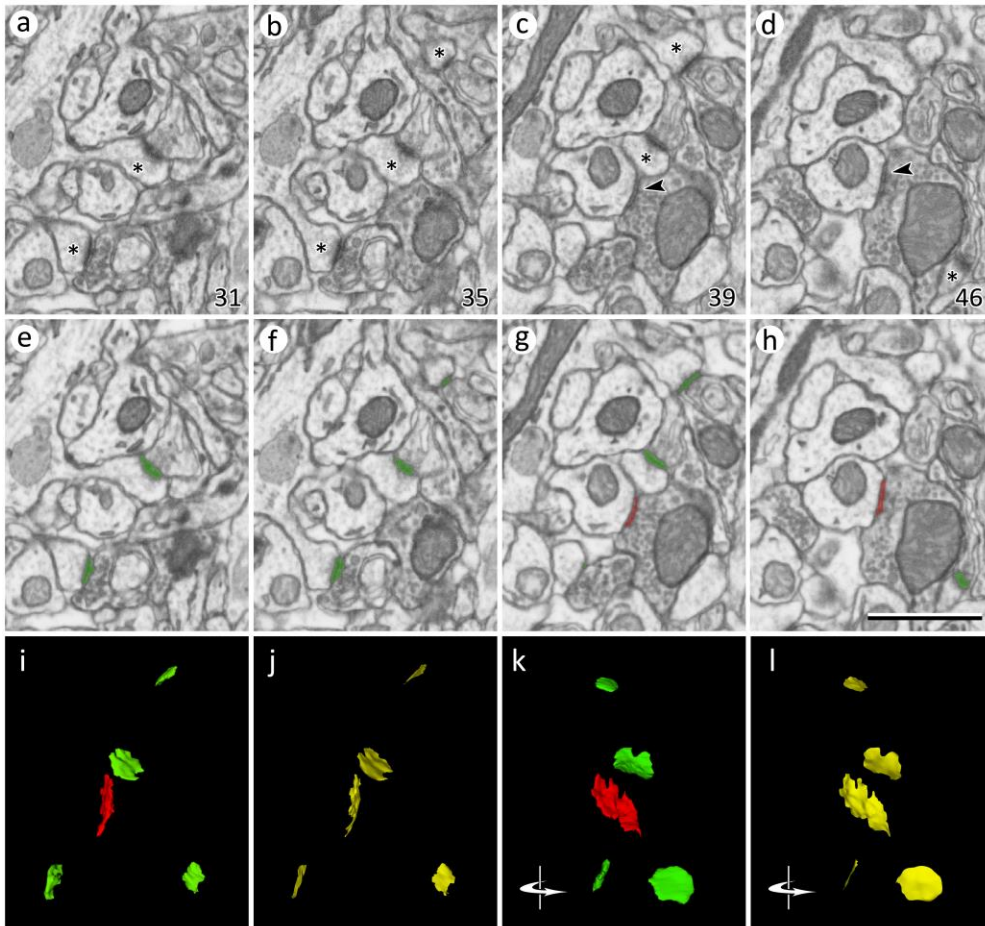
$$273 \quad dTotal = dPSD95 + dSAP102 - (c \times dTotal)$$

274 from which we obtain:

$$275 \quad dTotal = \frac{dPSD95 + dSAP102}{1 + c}$$

276 We observed the highest total density of puncta in SR (mean \pm SD; 145.18 ± 25.62 puncta/100
277 μm^2), followed by SO (140.75 ± 17.24 puncta/100 μm^2) and SLM (106.44 ± 17.64 puncta/100
278 μm^2) (Table 1, Supplementary Table 2). The differences between SLM and the other two layers
279 were statistically significant (KW test, $p < 0.005$) (Figure 5a).

280



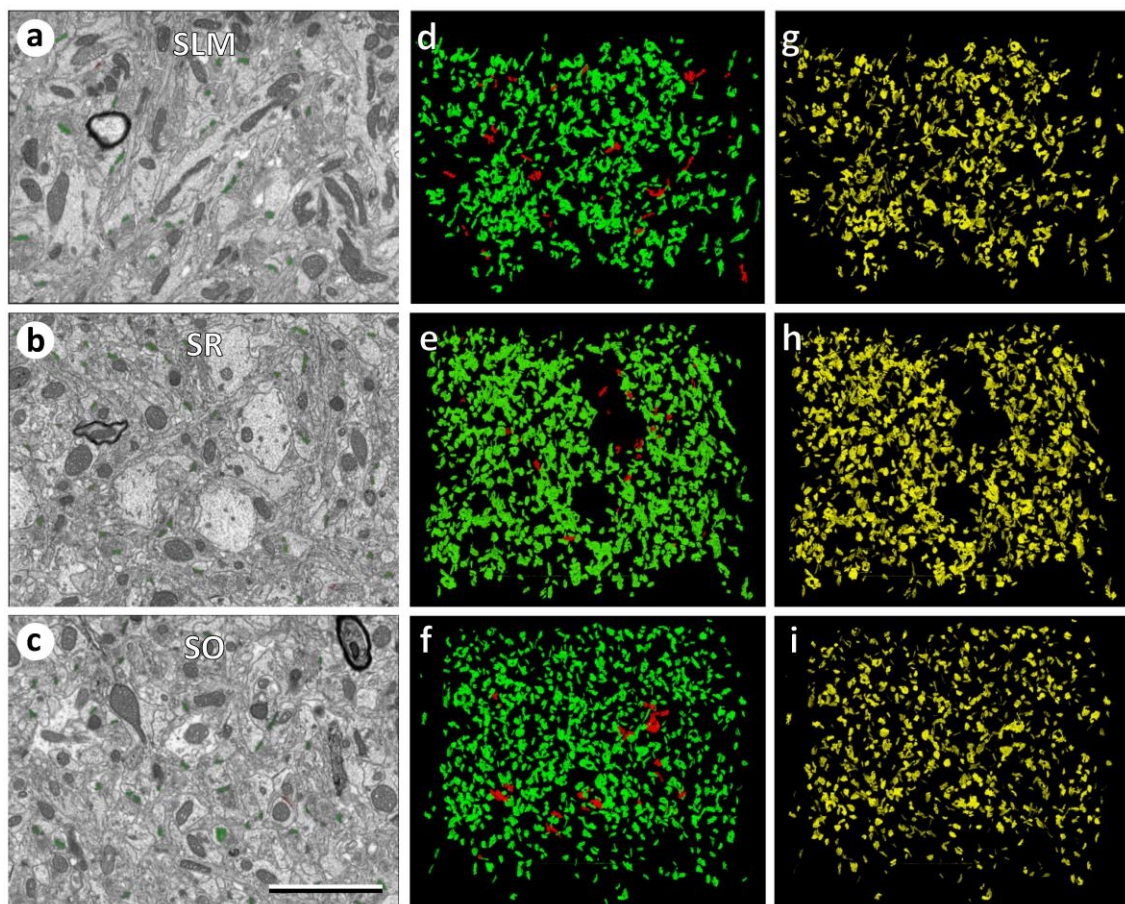
281

282 **Figure 3. Identification and segmentation of synaptic junctions in serial sections acquired by FIB-SEM.**
283 (a-c) Detail of four electron micrographs selected from a series of images obtained by FIB-SEM. In this
284 example, the stack of images was obtained from the stratum oriens. The numbers in the bottom-right
285 corner correspond to section number. Four asymmetric synapses can be identified by the presence of
286 prominent post-synaptic densities in (a), (b), (c) and (d) (asterisks). One symmetric synapse, with a thin
287 post-synaptic density, can be seen in (c) and (d) (arrow heads). Note that the classification of synapses

288 as asymmetric or symmetric is not based on single images but on the examination of the full sequence
289 of images. **(e-h)** The same images after they have been segmented with Espina software
290 (<http://cajalbbp.es/espina/>). The segmentation process is based on grey-level thresholds, so the
291 resulting 3D objects comprise both the pre- and post-synaptic densities (see methods). Green profiles
292 correspond to asymmetric synapses and red profiles to the symmetric synapse. **(i)** 3D rendering of the
293 synaptic junctions present in (a) to (h). **(j)** Synaptic apposition surfaces (SAS, yellow) extracted from the
294 3D segmentations represented in (i). SAS are automatically extracted from the 3D reconstructions of
295 synaptic junctions (see methods); they are zero-volume surfaces that represent the interface between
296 the pre- and post-synaptic densities. The surface area of the SAS is measured for each individual
297 synaptic junction. **(k, l)** Same structures represented in (i) and (j), respectively, after they have been
298 rotated through a vertical axis. Original images were acquired with a resolution of 5 nm/pixel, with a
299 distance of 20 nm between two consecutive images. Calibration bar in (h) is 1 μm .

300

301



302

303 **Figure 4. Measuring synaptic densities and sizes in stacks of sections obtained by FIB-SEM.** **(a-c)**
304 Panoramic view of electron micrographs of the stratum lacunosum moleculare (SLM), stratum radiatum
305 (SR) and stratum oriens (SO) imaged by FIB-SEM. **(d-f)** 3D rendering of synaptic junctions reconstructed
306 from the corresponding stacks of serial sections, acquired from the strata represented in (a) to (c).
307 Asymmetric synaptic junctions have been represented in green and symmetric synaptic junctions in red.
308 **(g-i)** The synaptic apposition surfaces (SAS, yellow) have been automatically extracted from the three-
309 dimensionally reconstructed synaptic junctions. The number of synapses per unit volume and the
310 surface areas of the SAS have been measured in each stack of serial sections (see Tables 1 and 2).
311 Calibration bar in (c): 3 μm .

312

313 For the volume electron microscopy study (FIB-SEM), we used 12 stacks of serial sections from
 314 SLM, SR and SO (Figure 3, Figure 4, Supplementary Table 1). In these samples, we identified
 315 and analyzed a total of 10,460 synapses in 4,905 μm^3 of tissue. Of these, 95.60% were AS and
 316 4.40% were SS. To estimate the density of synapses in each stack of images, we counted the
 317 number of synaptic junctions within an unbiased three-dimensional counting frame of known
 318 volume (see Methods). The density of AS (mean \pm SD) in SLM was 1.59 ± 0.73 synapses/ μm^3 , in
 319 SR it was 2.31 ± 0.38 synapses/ μm^3 , and in SO it was 2.49 ± 0.48 synapses/ μm^3 (Table 1).

320

321

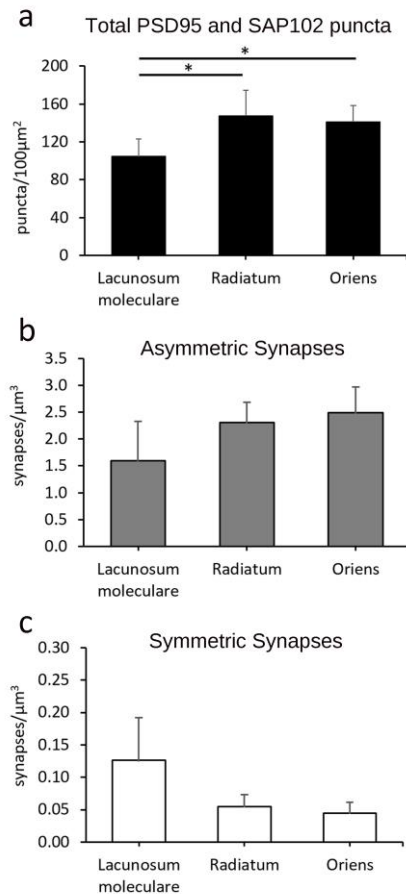
Stratum of CA1	Density of PSD95 (puncta/100 μm^2)	Density of SAP102 (puncta/100 μm^2)	Colocalization index	Total density of puncta/100 μm^2	Density of AS (synapses/ μm^3)	Conversion factor
Lacunosum-Moleculare	91.3103 \pm 13.3605	77.1788 \pm 23.8497	0.5840	106.4372 \pm 17.6450	1.5958 \pm 0.7317	0.0150
Radiatum	118.4513 \pm 25.8022	122.7022 \pm 24.2477	0.6633	145.1760 \pm 25.6250	2.3076 \pm 0.3788	0.0159
Oriens	119.7759 \pm 21.1004	115.6872 \pm 18.9181	0.6741	140.7479 \pm 17.2418	2.4887 \pm 0.4763	0.0177
All layers averaged	109.8458 \pm 24.2337	105.1894 \pm 29.8734	0.6404	130.7871 \pm 26.6441	2.1307 \pm 0.6396	0.0162

322

323 **Table 1. Relationship between the densities of puncta and the densities of synapses.** PSD95 and
 324 SAP102 puncta were imaged with SDM. The total densities of puncta were calculated from the densities
 325 of PSD95 and SAP102 puncta, together with the colocalization index (see text for details). The densities
 326 of asymmetric synapses (AS) were obtained from volumes of tissue reconstructed from serial sections
 327 using FIB-SEM. For each layer, the conversion factors is the quotient between the density of synapses
 328 obtained by FIB-SEM and the total density of puncta calculated from SDM images. Densities are given as
 329 average \pm SD

330

331 SS were most frequent in SLM (0.13 ± 0.07 synapses/ μm^3), followed by SR (0.06 ± 0.02
 332 synapses/ μm^3) and SO (0.05 ± 0.02 synapses/ μm^3). In spite of this trend of an increase in AS
 333 density from SLM to SO, and a decrease in SS across these strata, the differences between
 334 layers were not statistically significant for either the total density of synapses (AS+SS) or for AS
 335 and SS separately (KW test, $p \geq 0.08$) (Figure 5b, c).



336

337 **Figure 5. Total densities of PSD95 and SAP102 puncta, asymmetric synapses and symmetric synapses.**
 338 (a) Density of PSD95- and SAP102-positive puncta (puncta/100 µm² ± SD) acquired by SDM in the
 339 hippocampus (CA1). Asterisks indicate statistically significant differences (KW, p < 0.005). (b) and (c)
 340 Density of asymmetric and symmetric synapses, respectively (synapses/µm³ ± SD), estimated from
 341 stacks of serial sections acquired by FIB-SEM from the same regions. See also Table 1.

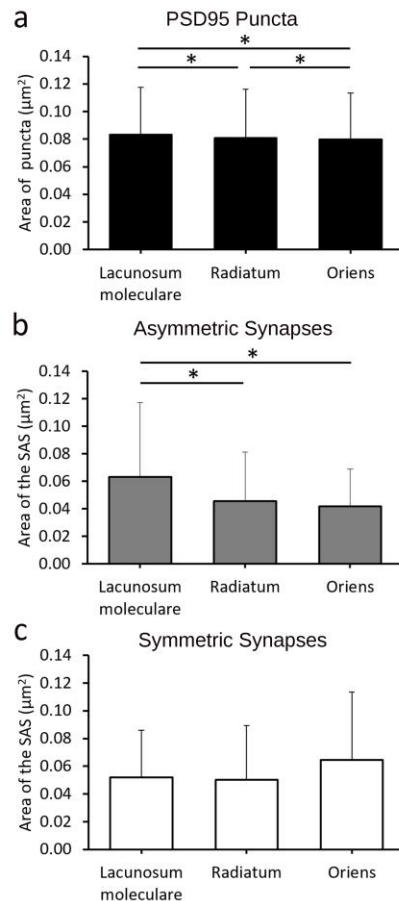
342

343 Size of fluorescent puncta and synapses in the hippocampus

344 We measured the area of PSD95 puncta in SLM, SR and SO. The largest mean area of puncta
 345 was found in SLM (0.0832 µm²), followed by SR (0.0809 µm²) and SO (0.0798 µm²) (Figure 6a).
 346 Although the differences were small, they were statistically significant (KW test p < 0.001).

347 To estimate the size of synapses in the FIB-SEM samples, we measured the area of the synaptic
 348 apposition surface (SAS). The SAS is a surface that represents the apposition between the
 349 presynaptic density and the PSD and reproduces their curvature (Figure 3, Figure 4, see
 350 Methods). The mean SAS area in the FIB-SEM samples was 0.0474 µm² for asymmetric
 351 synapses and 0.0541 µm² for symmetric synapses.

352 For asymmetric synapses, the mean SAS area in SLM was larger than in the other layers
 353 (0.0633 µm²; KW-Dunn's p < 0.001)(Figure 6b). Despite the mean SAS area being larger in SR
 354 than in SO (0.0456 µm² and 0.0419 µm², respectively), the difference was not statistically
 355 significant (KW-Dunn's p > 0.05). For symmetric synapses, the largest mean SAS areas were
 356 found in SO (0.0644 µm²) followed by SLM (0.0519 µm²) and SR (0.0501 µm²) (KW, p = 0.05)
 357 (Figure 6c, Table 2).



358

359 **Figure 6. Size of PSD95 puncta, asymmetric synapses and symmetric synapses.** (a) Area of PSD95-
360 positive puncta (μm^2) acquired by SDM in the hippocampus (CA1) (Mean + SD). Asterisks indicate
361 statistically significant differences. (b) and (c) Mean size of the synaptic apposition surface (SAS) of
362 asymmetric and symmetric synapses (μm^2) estimated from stacks of serial sections acquired by FIB-SEM
363 from the same region. See also Table 2.

364

365 When we compared the sizes of asymmetric synapses and symmetric synapses in different
366 layers, we found that symmetric synapses were larger than asymmetric synapses in SO and SR,
367 while in SLM the opposite was the case. The greatest differences were found in SO, where
368 mean SAS areas for symmetric synapses and asymmetric synapses were in a proportion of
369 approximately 6:4 (MW test, $p < 0.0001$) (Table 2).

370 To further characterize the size distribution of synaptic sizes, we plotted the frequency
371 histograms of the areas of PSD95 puncta and of the SAS (Figure 7). The frequency histograms
372 of the areas of PSD95 puncta showed skewed shapes, with a long tail to the right. The
373 histograms of SAS areas of asymmetric synapses measured from FIB-SEM reconstructions also
374 showed skewed shapes, but they were narrower and lay to the left of PSD95 histograms in all
375 layers (Figure 7).

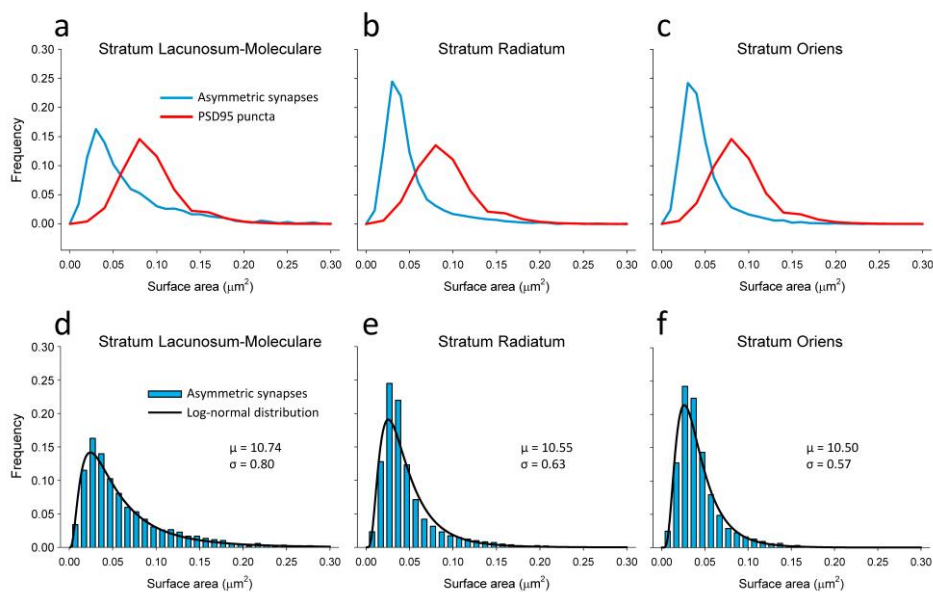
376 We then performed goodness-of-fit tests to find the theoretical probability density functions
377 that best fitted the empirical distributions of the areas of PSD95 puncta and SAS areas. We
378 found that they fitted to log-normal distributions in all cases, with some variations in the
379 parameters μ and σ (Table 2 and Figure 7).

		Stratum			
		Lacunosum-Moleculare	Radiatum	Oriens	All layers
PSD 95 Puncta	Mean Area \pm SD (μm^2)	0.0832 ± 0.0342	0.0809 ± 0.0352	0.0798 ± 0.0336	0.0813 ± 0.0342
	n	147776	189945	125916	463637
	μ	11.24	11.20	11.20	11.21
	δ	0.44	0.48	0.46	0.46
AS	Mean SAS Area \pm SD (μm^2)	0.0633 ± 0.0540	0.0456 ± 0.0358	0.0419 ± 0.0271	0.0474 ± 0.0377
	n	2258	4538	5082	11878
	μ	10.74	10.55	10.50	10.54
	δ	0.80	0.63	0.57	0.64
SS	Mean SAS Area \pm SD (μm^2)	0.0520 ± 0.0338	0.0501 ± 0.0394	0.0644 ± 0.0491	0.0541 ± 0.389
	n	247	93	87	427
	μ	10.67	10.60	10.97	10.70
	δ	0.68	0.65	0.75	0.69

380

381 **Table 2. Surface areas of PSD95 puncta acquired by SDM, and surface areas of the synaptic apposition**
 382 **surface (SAS) of asymmetric (AS) and symmetric (SS) synapses reconstructed from FIB-SEM samples.**
 383 The number of puncta or synapses analyzed (n), as well as the parameters μ and σ of the corresponding
 384 best-fit log-normal distributions are also indicated.

385



386

387 **Figure 7. Frequency histograms of the sizes of PSD95 puncta and asymmetric synapses. (a-c)**
 388 Comparison of the distribution of the surface areas of PSD95 puncta acquired by SDM (red line) and the
 389 synaptic apposition surfaces of asymmetric synapses reconstructed from FIB-SEM samples (blue line)
 390 from three layers of the CA1 region of the hippocampus. The histograms corresponding to asymmetric
 391 synapses are narrower and lie to the left of the histograms corresponding to PSD95 puncta. (d-f)
 392 Frequency histograms (blue bars) of the areas of the synaptic apposition surfaces of asymmetric
 393 synapses reconstructed from FIB-SEM samples. The log-normal distributions (black lines) represent the
 394 theoretical probability density functions that best fit the experimental data. The parameters μ and σ
 395 of the corresponding log-normal distributions have also been indicated.

396

397 **Brain-wide estimations of the number of synapses**

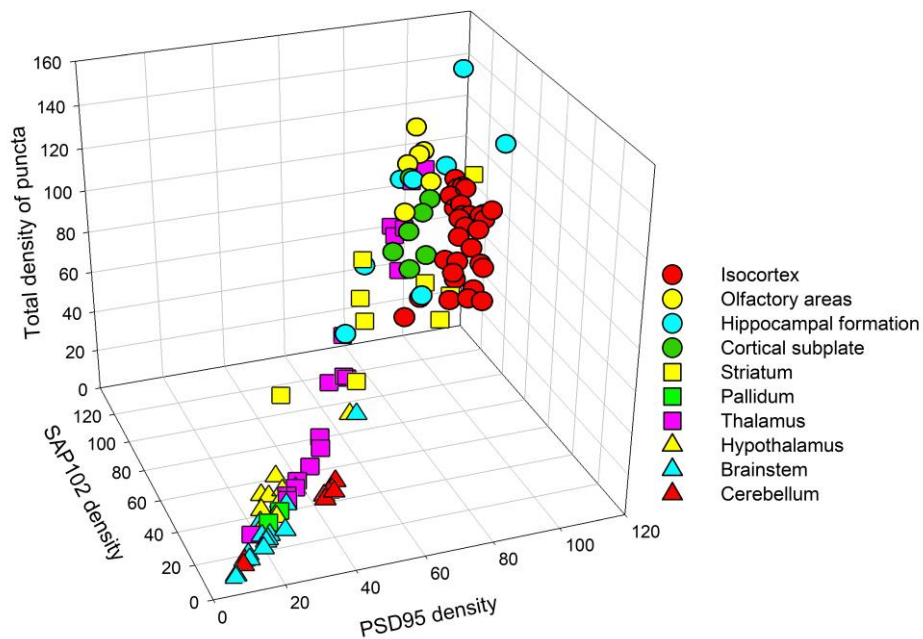
398 When we compared the densities of PSD95 and SAP102 puncta measured with SDM and the
399 densities of AS measured with FIB-SEM, we found that both methods revealed that SR and SO
400 had similar densities, while SLM had a lower density (Figure 5). We then calculated a
401 conversion factor that would allow us to relate the densities of PSD95 and SAP102 puncta
402 (puncta/100 μm^2) to the actual densities of excitatory synapses found by FIB-SEM
403 (synapses/ μm^3). These conversion factors were calculated as the quotient between the actual
404 density of AS and the total density of PSD95 and SAP102 puncta. Conversion factors obtained
405 for each layer of CA1 were slightly different; they ranged from 0.0152 to 0.0176. The averaged
406 conversion factor calculated with data from the three layers was 0.0162 (Table 1).

407 The next step was to calculate the total number of puncta expressing PSD95 and/or SAP102
408 brain-wide, using previously published data from 113 areas (Zhu et al., 2018). Different brain
409 regions had different combinations of densities of PSD95, SAP102 and total densities of puncta
410 (Figure 8, Supplementary Table 2). The highest total densities of puncta were found in the
411 isocortex, the olfactory areas, the hippocampal formation and the cortical subplate. All these
412 regions were relatively homogeneous except for the hippocampal formation, which showed
413 wider ranges of variability. Also, isocortical areas had a relatively higher proportion of PSD95
414 versus SAP102 than the other regions. The pallidum, the hypothalamus, the brainstem and the
415 cerebellum had low densities of puncta. Finally, the striatum —and especially the thalamus—
416 showed the greatest variability. For example, of all thalamic nuclei, the ventral medial nucleus
417 had one of the lowest estimated densities of total puncta (19.78 puncta/100 μm^2), while the
418 posterior complex had one of the highest estimated densities (110.15 puncta/100 μm^2)
419 (Supplementary Table 2). As a validation step, we compared previously published data
420 regarding CA1 (Zhu et al., 2018) with our present data; the total densities of puncta expressing
421 PSD95 and/or SAP102 were remarkably similar (128.95 puncta/100 μm^2 in previously published
422 data and 130.96 puncta/100 μm^2 in the present study).

423

424

425



426

427 **Figure 8. Densities of PSD95 and SAP102 puncta, and total densities of puncta in different**
428 **regions of the brain.** The total densities of puncta have been calculated from previously
429 published densities and colocalization indexes of PSD95 and SAP102 puncta (Zhu et al., 2018).
430 Symbols represent the different subregions within the major brain regions listed in the legend
431 (see Supplementary Table 2 for the complete list of subregions). The isocortex, the olfactory
432 areas, the hippocampal formation and the cortical subplate have high densities of puncta. The
433 pallidum, the hypothalamus, the brainstem and the cerebellum have low densities of puncta.
434 There is a wide variability in the total densities of puncta in the striatum and thalamus.

435

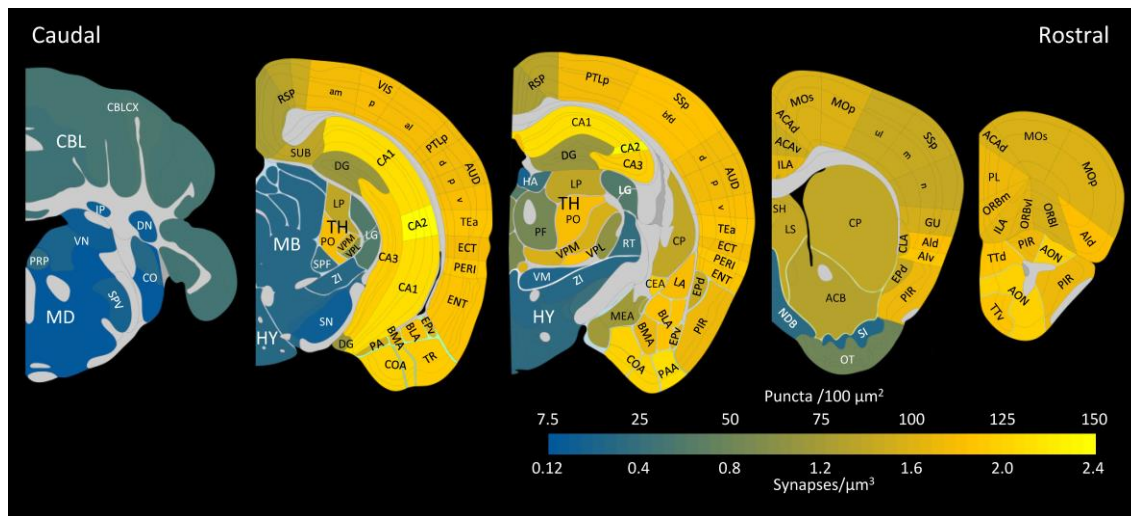
436

437 Finally, we estimated the density of synapses expressing PSD95 and/or SAP102, making use of
438 the averaged conversion factor obtained in CA1 (Table 1). The values obtained have been
439 graphically represented in Figure 9. In general, the hippocampal cornu ammonis, the isocortex
440 and the olfactory areas had the highest synaptic densities, intermingled with cortical subplate
441 nuclei. Within the hippocampal formation, the dentate gyrus and the subiculum presented
442 similar densities, but these were lower than in the Ammon's horn. Striatal nuclei showed
443 considerable variations, but the thalamic nuclei showed the highest variability, as mentioned
444 above. The cerebellar cortex showed homogeneously low densities and the pallidum,
445 hypothalamus and brainstem had the lowest synaptic densities.

446

447

448



449

450 **Figure 9. Estimated densities of synapses expressing PSD95 and/or SAP102 in different regions of the**
451 **brain.** The total densities of puncta per 100 square microns have been calculated from previously
452 published densities of PSD95 and SAP102, as well as their colocalization indexes (Zhu et al., 2018). A
453 conversion factor obtained in CA1 was used to estimate the minimum densities of synapses per cubic
454 micron (see text for details). Illustrations and brain regions are based on the Allen Mouse Brain Atlas.
455 The following structures have been labeled: **Cerebellum** (CBL), CBLCX: cerebellar cortex; DN: Dentate
456 nucleus; IP: Interposed nucleus. **Medulla** (MD), CO: Cochlear nuclei; PRP: Nucleus prepositus; SPV:
457 Spinal nucleus of the trigeminal; VN: Vestibular nuclei. **Midbrain** (MB), SN: Substantia nigra.
458 **Hypothalamus** (HY), ZI: Zona incerta. **Thalamus** (TH), HA: Habenular nuclei; LG: Lateral geniculate
459 complex; LP: Lateral posterior nucleus; PF: Parafascicular nucleus; PO: Posterior complex; RT: Reticular
460 nucleus; SPF: Suprafascicular nucleus; VM: Ventral medial nucleus; VPL: Ventral posterolateral nucleus;
461 VPM: Ventral posteromedial nucleus. **Pallidum**, NDB: Diagonal band nucleus; SI: Substantia innominata.
462 **Striatum**, ACB: Nucleus accumbens; CEA: Central amygdalar nucleus; CP: Caudoputamen; LS: Lateral
463 septal nucleus; MEA: Medial amygdalar nucleus. OT: Olfactory tubercle; SH: septohippocampal nucleus.
464 **Cortical subplate**, BLA: Basolateral amygdalar nucleus; BMA: Basomedial amygdalar nucleus; CLA:
465 Claustrium; EPd: Endopiriform nucleus, dorsal part; EPv: Endopiriform nucleus, ventral part; LA: Lateral
466 amygdalar nucleus; PA: Posterior amygdalar nucleus. **Olfactory areas**, AON: Anterior olfactory nucleus;
467 COA: Cortical amygdalar area; PAA: Piriform-amygdalar area; PIR: Piriform area; TR: Postpiriform
468 transition area; TTd: Taenia tecta, dorsal part; TTv: Taenia tecta, ventral part. **Hippocampal formation**,
469 CA1, CA2, CA3: Cornu Ammonis, fields 1, 2 and 3; DG: Dentate gyrus. ENT: Entorhinal area; SUB:
470 Subiculum. **Isocortex**, ACAd: Anterior cingulate area, dorsal part; ACAv: Anterior cingulate area, ventral
471 part; Ald: Agranular insular area, dorsal part; Alv: Agranular insular area, ventral part; AUD: Auditory
472 areas (d, p, v: dorsal, primary ventral); ECT: Ectorhinal area; GU: Gustatory area; ILA: Infralimbic area;
473 MOp: Primary motor area; MOs: Secondary motor area; ORBl: Orbital area, lateral part; ORBm: Orbital
474 area, medial part; ORBvl: Orbital area, ventrolateral part; PERI: Perirhinal area; PL: Prelimbic area; PTLp:
475 Posterior parietal association areas; RSP: Retrosplenial area; SSsp: Primary somatosensory area (bfd, ul
476 m, and n: barrel field, upper limb, mouth and nose representations); TEa: Temporal association areas;
477 VIS: Visual areas (am, p, al: anteromedial, primary, anterolateral).

478

479

480 Discussion

481 In this study, we have —for the first time— analyzed the synaptic density of excitatory and
482 inhibitory synapses, as well as their size, in stratum oriens, stratum radiatum and stratum
483 lacunosum-moleculare of the CA1 hippocampal region of the mouse, using three-dimensional
484 electron microscopy. With this method, long series of consecutive sections are obtained by
485 FIB-SEM, so individual synapses can be unambiguously identified and the number of synapses
486 per unit volume can be directly calculated. However, as with any other electron-microscopy
487 technique, FIB-SEM can only be applied to relatively small regions of tissue, so it is not
488 practical for brain-wide estimations. By contrast, the number of fluorescent puncta expressing
489 PSD95 and/or SAP102 can be quantified brain-wide using SDM, so we have attempted to
490 establish a correlation between the two kinds of measurements.

491 Synaptic sizes and densities in the hippocampus

492 Regarding the size of fluorescent puncta and PSDs, what is actually measured with SDM
493 imaging is different to what is measured after reconstruction of synaptic junctions from serial
494 images obtained by FIB-SEM. In the case of SDM, the images obtained are two-dimensional, so
495 what we actually see is the two-dimensional projection of puncta on the plane of section.
496 Thus, puncta with different orientations will show different apparent surface areas, and only
497 those that are oriented flat with respect to the plane of section will show their true surface
498 area. By contrast, serial images obtained by FIB-SEM allow us to reconstruct the synaptic
499 junctions in 3D. We can then extract the synaptic apposition surface (SAS) from each individual
500 synapse. The SAS represents the surface of apposition between the presynaptic and
501 postsynaptic densities, so the surface area of the SAS is equivalent to the area of the PSD, and
502 we can measure it for every synapse, regardless of its spatial orientation (Morales et al., 2013).

503 We have found that SDM imaging clearly overestimates the size of PSD95 puncta when
504 compared with the actual size of PSDs imaged by FIB-SEM (see Figure 7). This can be due to
505 several factors. Light scatter, glare and blur may contribute to the fact that fluorescent puncta
506 appear to be larger than the actual PSDs. The resolution of SDM is also much lower than the
507 resolution of electron microscopy. In the x-y plane, the resolution of SDM was 84 nm/pixel,
508 while FIB-SEM images were acquired at a resolution of 5 nm/pixel. This makes a pixel area of
509 7056 nm² for SDM versus only 25 nm² for FIB-SEM. The lower resolution may result in SDM
510 missing the smaller synapses and those that are oriented perpendicularly to the plane of
511 section. Also, the images of several synapses may overlap throughout the thickness of the SDM
512 optical section. As a result, some puncta may in fact be clusters of two or more synapses. In
513 spite of these differences between the two-dimensional SDM imaging and volume electron
514 microscopy, the measurements of fluorescent puncta by SDM do distinguish the relative size
515 differences between layers or regions, so they are still useful for the identification and
516 classification of synaptic types (Zhu et al., 2018). Both our SDM and FIB-SEM results indicate
517 that excitatory synapses in SLM are larger than in the SR or SO, in line with previous studies in
518 the rat (Megías et al., 2001).

519 The distribution of synaptic sizes measured from FIB-SEM stacks of images fits a log-normal
520 distribution in the three strata analyzed (see Figure 7d-f). This trait has also been described in
521 the rat neocortex (Merchán-Pérez et al., 2014; Santuy et al., 2018b). This type of distribution is
522 characterized by a skewed curve with a long tail to the right, and it has been found in other
523 synaptic parameters such as synaptic strength, spike transmission probability, and the size of

524 unitary excitatory postsynaptic potentials (Buzsáki and Mizuseki, 2014; Lefort et al., 2009; Song
525 et al., 2005; Hazan and Ziv, 2020). It is thus tempting to suggest that the size of the synaptic
526 junction is correlated with these and other functional characteristics of the synapse, as has
527 been proposed previously (Santuy et al., 2018b).

528 Regarding the densities of puncta and synapses in the hippocampus, previous studies in the rat
529 SR reported 2.2 synapses/ μm^3 using EM and three-dimensional reconstructions (Mishchenko
530 et al., 2010), and similar estimates using stereological methods (Sorra et al., 1998). In both
531 cases, the reported synapse densities were lower than the density we have found in the mouse
532 SR (2.4 synapses/ μm^3). Differences between species may explain the discrepancies, although
533 we cannot rule out the possibility of other sources of bias, such as the different methods used.
534 On the other hand, our SDM results regarding the total density of PSD95 and SAP102 puncta in
535 the hippocampus were very similar to previously reported data (Zhu et al., 2018). We also
536 provide information about the amount of inhibitory synapses, represented by symmetric or
537 type 2 synapses (Colonnier, 1968; Gray, 1959). These do not express PSD95 or SAP102, so their
538 densities cannot be estimated from our SDM data. However they can be identified in FIB-SEM
539 images because of their thin PSD (Merchán-Pérez et al., 2009). In our CA1 samples, symmetric
540 synapses represented 4.4% of the total number of synapses. This is in line with results in SR
541 and SO of the rat CA1, where percentages of inhibitory synapses as low as 3% have been
542 reported in thin dendrites, which predominate in our samples (Megías et al., 2001).
543 Interestingly, they also reported that—in line with our results— SLM had the highest
544 percentage of inhibitory synapses (leaving aside the stratum pyramidale and the thick proximal
545 dendrites, which were not included in our study).

546 **Brain-wide estimations of the minimum densities of synapses**

547 We next applied a conversion factor obtained in the hippocampus to calculate synaptic
548 densities brain-wide. The conversion factor was calculated as the ratio between the densities
549 of excitatory (asymmetric) synapses obtained by FIB-SEM and the total density of PSD95 and
550 SAP102 puncta obtained by SDM. We found that the conversion factors were very similar in
551 the three CA1 layers studied, and we used an averaged conversion factor for brain-wide
552 estimations (see Table 1). It is important to bear in mind the limitations of this procedure to
553 ensure that the results are interpreted correctly.

554 While it is clear that only excitatory glutamatergic synapses express PSD95 and/or SAP102
555 (Nithianantharajah et al., 2013; Frank et al., 2017; Zhu et al., 2018), the question of whether *all*
556 excitatory synapses express these scaffolding proteins does not have a simple answer. In the
557 adult mouse hippocampus, it has been recently claimed that all Schaffer
558 collateral/commissural synapses in the SR of CA1 show immunogold staining for PSD95
559 (Yamasaki et al., 2016). This is probably an overestimate, since our own data indicate that
560 there is a population of synapses that do not express PSD95, but do express SAP102
561 (Supplementary Table 2). In any case, if we consider that Schaffer collateral/commissural fibers
562 are the origin of the vast majority of synapses in SR and SO, we can assume that most, if not
563 all, synapses in these strata express PSD95, SAP102 or a combination of the two. It is likely to
564 be the same case in SLM, since the ratio between the number of fluorescent puncta and the
565 actual density of synapses measured by FIB-SEM is very similar to that of the two other layers
566 (see Table 1). Lower percentages of immunolabeling of synapses with PSD95 have been
567 reported in the rat hippocampus (Sans et al., 2000), but this has been attributed to the low
568 sensitivity of the technique (Sassoé-Pognetto et al., 2003). In our case, the advantage of the

569 genetic labeling method is that all PSD95 and SAP102 proteins are labeled, so a more reliable
570 detection is to be expected.

571 However, even if we assume that the vast majority of excitatory synapses in CA1 express
572 PSD95 and/or SAP102, and that we can detect them in a reliable way, the question remains as
573 to whether this would be the case in other brain regions. For example, PSD95 was regarded as
574 “a fundamental structural component of most, if not all, excitatory PSDs isolated from the rat
575 cerebral cortex” (Petersen et al., 2003). Other studies seem to confirm this view (Swulius et al.,
576 2010; DeGiorgis et al., 2006), while lower percentages of PSD95-expressing synapses have also
577 been reported (Aoki et al., 2001; Farley et al., 2015). Brain-wide studies in the mouse seem to
578 confirm that the abundance of scaffolding proteins like PSD95 and SAP102 differs depending
579 on the brain area (Roy et al., 2018; Zhu et al., 2018). Also, although PSD95 and SAP102
580 together are thought to label most excitatory synapses, we expect that labeling with PSD93
581 could reveal an additional set of excitatory synapses (Elias et al., 2006). Finally, the vast
582 majority of PSD95 puncta in the adult brain are found in the postsynaptic terminals, but they
583 have also been observed in non-synaptic locations in developing neurons (Gerrow et al., 2006;
584 Washbourne et al., 2002). Thus, we cannot rule out the possibility that some of the PSD95
585 puncta observed in the adult mouse brain are not from extra-synaptic sites.

586 Therefore, to interpret our results correctly, we must clearly assume that not all excitatory
587 synapses throughout the brain express PSD95 and/or SAP102. Since our calculations are based
588 only on the population of synapses that express these scaffolding proteins, our estimations of
589 synaptic densities do in fact underestimate the actual densities of excitatory synapses. In other
590 words, our estimations represent the lower boundary of the densities of excitatory synapses in
591 different brain regions. The upper boundary cannot be estimated from our present data, since
592 this would require knowing the proportion of excitatory synapses that *do not* express PSD95
593 and/or SAP102 in each brain region.

594 Only a systematic exploration of the different regions of the brain with FIB-SEM or similar
595 methods will settle the possible discrepancies between our present estimations and the actual
596 values. However, we can compare our estimations with previous studies, when available. In
597 the mouse neocortex, previously reported synaptic densities using different stereological
598 methods were either lower (Sadaka et al., 2003; Schüz and Palm, 1989) or higher (DeFelipe et
599 al., 1997) than our present estimations. In the juvenile rat somatosensory cortex, the mean
600 density of synapses in the neuropil has been reported to be between 0.87 and 0.89
601 synapses/ μm^3 using FIB-SEM (Anton-Sanchez et al., 2014; Santuy et al., 2018a), which is below
602 our present estimation for the adult mouse somatosensory cortex (1.4 to 1.9 synapses/ μm^3 ,
603 see Supplementary Table 2). However, these differences may be due to species and/or age
604 differences (e.g., DeFelipe et al., 1997). In the rat cerebellum, the density of synapses has been
605 previously reported to be 0.8 synapses/ μm^3 in the molecular layer (Napper and Harvey, 1988),
606 while our present estimations for the mouse cerebellar cortex range from 0.5 to 0.6
607 synapses/ μm^3 (Supplementary Table 2). Therefore, we currently lack data that are directly
608 comparable to our present estimations, since methodological bias is probably at play in those
609 cases, leaving aside the possible species and age differences. Although work is already in
610 progress on the mouse somatosensory cortex using a FIB-SEM methodology that is similar to
611 the one presented here, it would not be practical to wait until results from even a fraction of
612 the 113 subregions examined here become available. Therefore, our calculations must be
613 regarded as reasonable—but provisional—estimations of the minimum densities of
614 glutamatergic synapses in the different brain regions.

615 In summary, it is important to emphasize that acquiring multiple samples at different scales is
616 a highly effective way to obtain a dataset that allows comprehensive analysis of the brain.
617 Since the whole brain cannot be fully reconstructed at the ultrastructural level, it seems clear
618 that only by combining studies at the meso- and nano-scopic levels (light and electron
619 microscopy) can we fully understand the structural arrangement of the brain as a whole [see,
620 for example (Markram et al., 2015, Kashiwagi et al., 2019)]. Using this strategy, we provide an
621 estimation of the minimum densities of glutamatergic synapses in the different brain regions.
622 These data, in combination with previous studies on the relationship between the connectome
623 and synaptome (Zhu et al., 2018), can be used to identify common and differing principles of
624 synaptic organization. This in turn could serve to further advance efforts to validate and refine
625 realistic brain models.

626

627

628

629 **Acknowledgements**

630 This work was supported by grants from the following entities: the Spanish “Ministerio de
631 Ciencia, Innovación y Universidades” (grant PGC2018-094307-B-I00 and the Cajal Blue Brain
632 Project [C080020-09; the Spanish partner of the Blue Brain Project initiative from EPFL,
633 Switzerland]; the European Union’s Horizon 2020 Research and Innovation Programme under
634 grant agreement No. 785907 (Human Brain Project, SGA2); the Wellcome Trust (Technology
635 Development Grant 202932); and the European Research Council (ERC) under the European
636 Union’s Horizon 2020 research and innovation programme (695568 SYNNOVATE). L.T.-R. is a
637 recipient of grants from the EMBO Long-term fellowship 2016–2018 and the IBRO-PERC
638 InEurope grants programme.

639

640 References

- 641 Anton-Sanchez L, Bielza C, Merchan-Perez A, Rodríguez J-R, DeFelipe J, Larrañaga P (2014) Three-
642 dimensional distribution of cortical synapses: a replicated point pattern-based analysis. *Front*
643 *Neuroanat* 8:85.
- 644 Aoki C, Miko I, Oviedo H, Mikeladze-Dvali T, Alexandre L, Sweeney N, Brecht DS (2001) Electron
645 microscopic immunocytochemical detection of PSD-95, PSD-93, SAP-102, and SAP-97 at
646 postsynaptic, presynaptic, and nonsynaptic sites of adult and neonatal rat visual cortex.
647 *Synapse* 40:239–257.
- 648 Buzsáki G, Mizuseki K (2014) The log-dynamic brain: how skewed distributions affect network
649 operations. *Nat Rev Neurosci* 15:264–278.
- 650 Chen X, Winters C, Azzam R, Li X, Galbraith JA, Leapman RD, Reese TS (2008) Organization of the core
651 structure of the postsynaptic density. *PNAS* 105:4453–4458.
- 652 Chen X, Winters C, Crocker V, Lazarou M, Sousa AA, Leapman RD, Reese TS (2018) Identification of PSD-
653 95 in the Postsynaptic Density Using MiniSOG and EM Tomography. *Front Neuroanat* 12.
- 654 Colonnier M (1968) Synaptic patterns on different cell types in the different laminae of the cat visual
655 cortex. An electron microscope study. *Brain Res* 9:268–287.
- 656 DeFelipe J, Fairén A (1993) A simple and reliable method for correlative light and electron microscopic
657 studies. *J Histochem Cytochem* 41:769–772.
- 658 DeFelipe J, Marco P, Busturia I, Merchán-Pérez A (1999) Estimation of the number of synapses in the
659 cerebral cortex: methodological considerations. *Cereb Cortex* 9:722–732.
- 660 DeFelipe J, Marco P, Fairén A, Jones EG (1997) Inhibitory synaptogenesis in mouse somatosensory
661 cortex. *Cereb Cortex* 7:619–634.
- 662 DeGiorgis JA, Galbraith JA, Dosemeci A, Chen X, Reese TS (2006) Distribution of the scaffolding proteins
663 PSD-95, PSD-93, and SAP97 in isolated PSDs. *Brain Cell Biology* 35:239–250.
- 664 Elias GM, Funke L, Stein V, Grant SG, Brecht DS, Nicoll RA (2006) Synapse-specific and developmentally
665 regulated targeting of AMPA receptors by a family of MAGUK scaffolding proteins. *Neuron*
666 52(2):307–320.
- 667 Farley M, Swilius M, Waxham M (2015) Electron Tomographic Structure and Protein Composition of
668 Isolated Rat Cerebellar, Hippocampal and Cortical Postsynaptic Densities. *Neuroscience*
669 304:286–301.
- 670 Frank RAW, Zhu F, Komiyama NH, Grant SGN (2017) Hierarchical organization and genetically separable
671 subfamilies of PSD95 postsynaptic supercomplexes. *J Neurochem* 142:504–511.
- 672 Gerrow K, Romorini S, Nabi SM, Colicos MA, Sala C, El-Husseini A (2006) A preformed complex of
673 postsynaptic proteins is involved in excitatory synapse development. *Neuron* 49(4):547–562.
- 674 Gray EG (1959) Axi-somatic and axo-dendritic synapses of the cerebral cortex: an electron microscope
675 study. *J Anat* 93:420–433.
- 676 Hafner A-S, Penn AC, Grillo-Bosch D, Retailliau N, Pujol C, Philippat A, Coussen F, Sainlos M, Opazo P,
677 Choquet D (2015) Lengthening of the Stargazin Cytoplasmic Tail Increases Synaptic
678 Transmission by Promoting Interaction to Deeper Domains of PSD-95. *Neuron* 86:475–489.
- 679 Hazan L, Ziv NE (2020) Activity dependent and independent determinants of synaptic size diversity. *J*
680 *Neurosci* 40:2828–2848
- 681 Howard CV, Reed MG (2005) Unbiased stereology : three-dimensional measurement in microscopy, 2nd
682 ed. ed. Oxon, UK: Garland Science/Bios Scientific Publishers.
- 683 Husi H, Ward MA, Choudhary JS, Blackstock WP, Grant SGN (2000) Proteomic analysis of NMDA
684 receptor–adhesion protein signaling complexes. *Nat Neurosci* 3:661–669.
- 685 Jeyifous O, Lin EI, Chen X, Antinone SE, Mastro R, Drisdell R, Reese TS, Green WN (2016) Palmitoylation
686 regulates glutamate receptor distributions in postsynaptic densities through control of PSD95
687 conformation and orientation. *PNAS* 113:E8482–E8491.
- 688 Kashiwagi Y, Higashi T, Obashi K, Sato Y, Komiyama NH, Grant SGN, Okabe S (2019) Computational
689 geometry analysis of dendritic spines by structured illumination microscopy. *Nat Commun*
690 10:1285.
- 691 Lefort S, Tomm C, Floyd Sarria J-C, Petersen CCH (2009) The Excitatory Neuronal Network of the C2
692 Barrel Column in Mouse Primary Somatosensory Cortex. *Neuron* 61:301–316.
- 693 Levy JM, Chen X, Reese TS, Nicoll RA (2015) Synaptic Consolidation Normalizes AMPAR Quantal Size
694 following MAGUK Loss. *Neuron* 87:534–548.

- 695 Markram H et al. (2015) Reconstruction and Simulation of Neocortical Microcircuitry. *Cell* 163:456–492.
- 696 Megías M, Emri Z, Freund TF, Gulyás AI (2001) Total number and distribution of inhibitory and excitatory
697 synapses on hippocampal CA1 pyramidal cells. *Neuroscience* 102:527–540.
- 698 Merchán-Pérez A, Rodríguez J-R, Alonso-Nanclares L, Schertel A, Defelipe J (2009) Counting synapses
699 using FIB/SEM microscopy: a true revolution for ultrastructural volume reconstruction. *Front*
700 *Neuroanat* 3:18.
- 701 Merchán-Pérez A, Rodríguez J-R, González S, Robles V, Defelipe J, Larrañaga P, Bielza C (2014) Three-
702 dimensional spatial distribution of synapses in the neocortex: a dual-beam electron microscopy
703 study. *Cereb Cortex* 24:1579–1588.
- 704 Migaud M, Charlesworth P, Dempster M, Webster LC, Watabe AM, Makhinson M, He Y, Ramsay MF,
705 Morris RGM, Morrison JH, O’Dell TJ, Grant SGN (1998) Enhanced long-term potentiation and
706 impaired learning in mice with mutant postsynaptic density-95 protein. *Nature* 396:433–439.
- 707 Mishchenko Y, Hu T, Spacek J, Mendenhall J, Harris KM, Chklovskii DB (2010) Ultrastructural analysis of
708 hippocampal neuropil from the connectomics perspective. *Neuron* 67:1009–1020.
- 709 Morales J, Alonso-Nanclares L, Rodríguez J-R, DeFelipe J, Rodríguez Á, Merchán-Pérez A (2011) Espina: a
710 tool for the automated segmentation and counting of synapses in large stacks of electron
711 microscopy images. *Front Neuroanat* 5:18.
- 712 Morales J, Rodríguez A, Rodríguez J-R, DeFelipe J, Merchán-Pérez A (2013) Characterization and
713 extraction of the synaptic apposition surface for synaptic geometry analysis. *Front Neuroanat*
714 7:20.
- 715 Napper RMA, Harvey RJ (1988) Number of parallel fiber synapses on an individual Purkinje cell in the
716 cerebellum of the rat. *J Comp Neurol* 274:168–177.
- 717 Nithianantharajah J, Komiyama NH, McKechnie A, Johnstone M, Blackwood DH, St Clair D, Emes RD,
718 van de Lagemaat LN, Saksida LM, Bussey TJ, Grant SG (2013) Synaptic scaffold evolution
719 generated components of vertebrate cognitive complexity. *Nat Neurosci* 16:16–24.
- 720 Paxinos G, Franklin KB (2004) The mouse brain in stereotaxic coordinates. Gulf Professional Publishing.
- 721 Petersen JD, Chen X, Vinade L, Dosemeci A, Lisman JE, Reese TS (2003) Distribution of Postsynaptic
722 Density (PSD)-95 and Ca²⁺/Calmodulin-Dependent Protein Kinase II at the PSD. *J Neurosci*
723 23:11270–11278.
- 724 Qiu Z, Yang L, Lu W (2012) A new feature-preserving nonlinear anisotropic diffusion for denoising images
725 containing blobs and ridges. *Pattern Recognition Letters* 33:319–330.
- 726 Roy M, Sorokina O, McLean C, Tapia-González S, DeFelipe J, Armstrong J, Grant S (2018) Regional
727 Diversity in the Postsynaptic Proteome of the Mouse Brain. *Proteomes* 6:31.
- 728 Sadaka Y, Weinfeld E, Lev DL, White EL (2003) Changes in mouse barrel synapses consequent to sensory
729 deprivation from birth. *J Comp Neurol* 457:75–86.
- 730 Sans N, Petralia RS, Wang Y-X, Blahos J, Hell JW, Wenthold RJ (2000) A Developmental Change in NMDA
731 Receptor-Associated Proteins at Hippocampal Synapses. *J Neurosci* 20:1260–1271.
- 732 Santuy A, Rodríguez J-R, DeFelipe J, Merchán-Pérez A (2018a) Volume electron microscopy of the
733 distribution of synapses in the neuropil of the juvenile rat somatosensory cortex. *Brain Struct*
734 *Funct* 223:77–90.
- 735 Santuy A, Rodríguez J-R, DeFelipe J, Merchán-Pérez A (2018b) Study of the Size and Shape of Synapses in
736 the Juvenile Rat Somatosensory Cortex with 3D Electron Microscopy. *eNeuro* 5:e0377-17.2017.
- 737 Sassoé-Pognetto M, Utvik JK, Camoletto P, Watanabe M, Stephenson FA, Brecht DS, Ottersen OP (2003)
738 Organization of postsynaptic density proteins and glutamate receptors in axodendritic and
739 dendrodendritic synapses of the rat olfactory bulb: PSD-95/PSD-93 in the Olfactory Bulb. *J*
740 *Comp Neurol* 463:237–248.
- 741 Schüz A, Palm G (1989) Density of neurons and synapses in the cerebral cortex of the mouse. *J Comp*
742 *Neurol* 286:442–455.
- 743 Song S, Sjöström PJ, Reigl M, Nelson S, Chklovskii DB (2005) Highly Nonrandom Features of Synaptic
744 Connectivity in Local Cortical Circuits. *PLoS Biology* 3:e68.
- 745 Sorra KE, Fiala JC, Harris KM (1998) Critical assessment of the involvement of perforations, spinules, and
746 spine branching in hippocampal synapse formation. *J Comp Neurol* 398:225–240.
- 747 Swulius MT, Kubota Y, Forest A, Waxham MN (2010) Structure and composition of the postsynaptic
748 density during development. *J Comp Neurol* 518:4243–4260.
- 749 Valtschanoff JG, Burette A, Wenthold RJ, Weinberg RJ (1999) Expression of NR2 receptor subunit in rat
750 somatic sensory cortex: Synaptic distribution and colocalization with NR1 and PSD-95. *Journal*
751 *of Comparative Neurology* 410:599–611.

- 752 Washbourne P, Bennett JE, McAllister AK (2002) Rapid recruitment of NMDA receptor transport packets
753 to nascent synapses. *Nat Neurosci* 5(8):751-759.
- 754 Yamasaki M, Fukaya M, Yamazaki M, Azechi H, Natsume R, Abe M, Sakimura K, Watanabe M (2016)
755 TARP γ -2 and γ -8 Differentially Control AMPAR Density Across Schaffer Collateral/Commissural
756 Synapses in the Hippocampal CA1 Area. *J Neurosci* 36:4296–4312.
- 757 Ye F, Zeng M, Zhang M (2018) Mechanisms of MAGUK-mediated cellular junctional complex
758 organization. *Curr Opin Struct Biol* 48:6–15.
- 759 Zhu F, Cizeron M, Qiu Z, Benavides-Piccione R, Kopanitsa MV, Skene NG, Koniaris B, DeFelipe J, Fransén
760 E, Komiyama NH, Grant SGN (2018) Architecture of the Mouse Brain Synaptome. *Neuron*
761 99:781-799.e10.
- 762 Zhu J, Shang Y, Zhang M (2016) Mechanistic basis of MAGUK-organized complexes in synaptic
763 development and signalling. *Nat Rev Neurosci* 17:209–223.
- 764